

Measurement of Temporal Coherence of Free Electrons by Time-Domain Electron Interferometry

M. Tsarev¹, A. Ryabov¹, and P. Baum^{1*}

Universität Konstanz, Universitätsstraße 10, 78464 Konstanz, Germany

 (Received 12 May 2021; revised 26 August 2021; accepted 16 September 2021; published 11 October 2021)

The temporal properties of an electron beam are decisive for modern ultrafast electron microscopy and for the quantum optics of the free electron in laser fields. Here, we report a time-domain interferometer that measures and distinguishes the pure and ensemble coherences of a free-electron beam in a transmission electron microscope via symmetry-breaking shifts of photon-order sideband peaks. This result is a free-electron analog to the reconstruction of attosecond bursts and photoemission delays in optical attosecond spectroscopy. We find a substantial pure electron coherence that is connected to the thermodynamics of the emitter material and a lower ensemble coherence that is governed by space-charge effects. Pure temporal coherences above 5 fs are measured at $>10^9$ electrons per second in a high-brightness beam.

DOI: [10.1103/PhysRevLett.127.165501](https://doi.org/10.1103/PhysRevLett.127.165501)

The wave nature of the electron has revolutionized modern material science and biology through a wealth of novel imaging techniques, for example, electron microscopy [1], holography [2], diffraction [3], tomography [4], or spectroscopy [5] at resolutions approaching subatomic dimensions. Recently, femtosecond and attosecond time resolution has been achieved as well [6–14], paving the way to seeing material transformations as a sequence of atomic and electronic motions in space and time [8,9]. Also, free-electron wave functions under control of the optical cycles of laser light [15–19] provide opportunities for time-gated imaging [15,20] and advanced investigations of quantum mechanics [21–23]. Critical for all such applications is the temporal coherence length of a free-electron beam, that is, the ability of the electron matter wave to interfere with a time-delayed part of itself. Often, temporal coherence is inferred from the inverse energy bandwidth via the uncertainty principle [24,25], resulting in values below one femtosecond. However, such values are not consistent with recent reports of coherent manipulations of electrons with laser light [13–16,26], where the observed electron interferences prove a coherent coverage of multiple laser cycles. Hence, the ability of electrons to interfere with themselves in the time domain cannot be deduced from a spectral measurement alone.

Here, we therefore differentiate the pure temporal coherence τ^{pure} of the electron wave function from the ensemble coherence τ^{ens} of the beam [25,27]. The associated energy bandwidths are $\sigma_E^{\text{pure}} \approx \hbar/(2\tau^{\text{pure}})$ and $\sigma_E^{\text{ens}} \approx \hbar/(2\tau^{\text{ens}})$, respectively. A finite τ^{pure} follows from the quantum mechanics of photoemission [24] and a finite τ^{ens} may be caused by space-charge effects [28,29], fluctuating acceleration voltages [24], electromagnetic fields [30], or electron-material interactions [31].

Consequently, an experimental dissection of pure and ensemble effects calls for a single-electron interferometer with ultrafast time resolution below the magnitudes of the expected coherences. Unlike Hasselbach *et al.* [32], who shifted and overlapped low-energy electron wave packets with a series of Wien filters, we measure here directly the subrelativistic electron beams in a transmission electron microscope and achieve the necessary attosecond resolution with laser radiation [14].

Figure 1(a) depicts the concept of our experiment. The electron beam (blue) interacts with the optical cycles of a coherent laser beam (red). Such an interaction converts the energy spectrum of the electron beam into a series of photon-order sidebands [14–16]. These sidebands are located at discrete energies $E_0 + N\hbar\omega$, where E_0 is the initial central electron energy, ω is the angular frequency of the laser wave and N is the sideband number [14–16]. After an extended propagation of the so-prepared electron wave function, we let the laser wave interact again and interlink the sidebands for a second time (multicolor arrows). The final energy spectrum is measured with an energy-resolving detector.

At the exit of the interferometer, each final sideband has two types of contributions: first, a *direct* wave packet that has propagated at the same energy all the time [path 1 in Fig. 1(a)], and second, two or more *detour* wave packets that have propagated between the two interactions at intermediate gains or losses of energy [paths 2 and 3 in Fig. 1(a)]. Figure 1(b) illustrates the resulting interference in the spectral domain. The energy envelopes of all final and intermediate sidebands are replicas of the initial energy envelope (solid lines), but *direct* and *detour* components have different spectral (energy-dependent) phases (dotted lines), because they have traveled the same physical distance at a different energy and therefore at a different

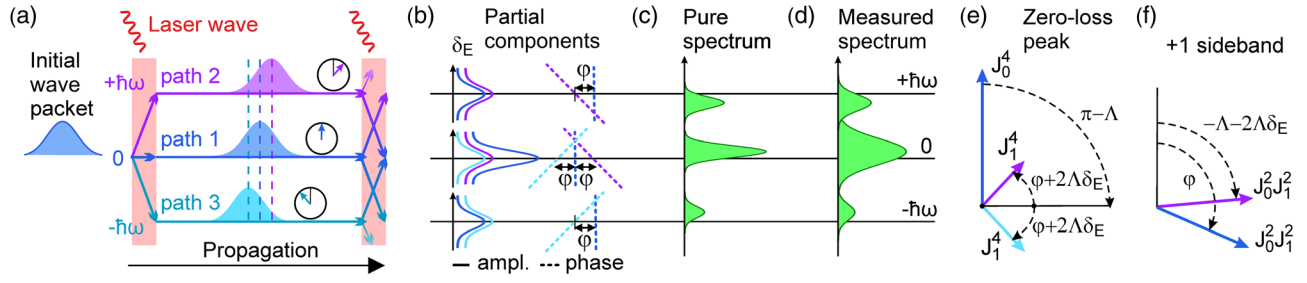


FIG. 1. Time-domain electron wave-packet interference leading to photon-order peak shifts. (a) Shaded regions mark the two interactions with the laser wave. After the first laser modulation, the wave packet consists of several energy components (cyan, blue, magenta). Propagation induces group and phase delays (bell shapes and clock symbols). The second laser modulation interlinks the energy states again and measures the phase delays. (b) Partial spectral components at $-\hbar\omega$, 0 , $\hbar\omega$ (cyan, blue, magenta) with their amplitudes (solid curves) and phases (dotted lines) after the second laser interaction. φ is the optical laser delay. (c) Resulting pure spectrum (green) with asymmetric energy-shifted sideband peaks. (d) Additional incoherent broadening preserves the peak shifts with respect to $-\hbar\omega$, 0 , $\hbar\omega$ (solid black lines). (e) Vector diagram for the summation of the partial components (color arrows) for the zero-loss peak according to Eq. (2). Solid arrows show the amplitudes and the dashed arrows the respective rotation phases. $J_0 = J_0(|g_{1,2}|)$ and $J_1 = J_1(|g_{1,2}|)$. (f) Analogous vector diagram for the +1 sideband.

dispersion. If the propagation time between the two laser interactions is very large, these dispersion differences become dominant over the absolute phase changes φ that usually simply turn a sideband on or off as a whole [26]. Consequently, there is now intraenvelope interference [see Fig. 1(c)]: higher-energy parts and lower-energy parts within a sideband obtain different intensities due to constructive spectral interference at the intersections of the spectral phases [dotted lines in Fig. 1(b)] and destructive interference otherwise. Therefore, measured spectral peak positions can shift away from the ladder of photon orders [14]. Importantly, the amount of peak shift and the widths of the sidebands will depend on the temporal coherences: τ^{pure} determines the sideband width and thereby the range of intrasideband energies that contribute to shifting the peak [see Fig. 1(c)] while τ^{ens} simply broadens all sideband peaks at no change of the peak shift [see Fig. 1(d)]. As a result, both τ^{ens} and τ^{pure} can be determined from the experiment.

For an analytical description, we consider an electron wave packet $\Psi(z, t) = \Psi_0(z', t) \exp[i(p_0 z - E_0 t)/\hbar]$ that propagates along the z direction with a velocity v_0 and a forward momentum p_0 . $\Psi_0(z', t)$ is the wave packet envelope, for example initially a Gaussian of width τ^{pure} according to $\Psi_0(z', 0) = A \exp[-z'^2/(2v_0\tau^{\text{pure}})^2]$, where A is the normalization constant and $z' = z - v_0 t$ is the local coordinate. This wave packet interacts twice with laser radiation, once at $z = 0$ and once substantially later at $z = L$. Solving the relativistic Schrödinger equation [33], we obtain the spectral envelope of the final electron wave function $\tilde{\Psi}_f(E, \varphi)$ after our two large-distance electron-laser interactions (see Supplemental Material [34] for derivation):

$$\tilde{\Psi}_f(E, \varphi) = \sum_{n,m} \tilde{\Psi}_N(E) P_{n,m} e^{im\varphi - i\Lambda(n^2 + 2n\delta_E)} \quad (1)$$

Here, E is the electron energy (E_0 subtracted), φ is the laser phase delay, n and m are integer numbers from $-\infty$ to ∞ that represent the number of photons absorbed at the first and second laser interaction, $N = n + m$ is the final sideband number, $\tilde{\Psi}_N(E)$ is the spectral envelope of the N th sideband, $P_{n,m} = J_n(|g_1|)J_m(|g_2|)$ are amplitudes or weight factors, $J_{n,m}$ are Bessel functions of the first kind, and $g_{1,2}$ are the coupling constants of the two laser-electron interactions [16]. The phases in Eq. (1) contain, first, the laser delay between the two interactions $\varphi = \arg g_2 - \arg g_1$ and, second, a multiplier $\Lambda = L\hbar\omega^2/(2v_0^3\gamma^3 m_e)$ that is proportional to the distance L between the interactions; m_e is the electron mass and γ is the Lorentz factor. We have introduced in Eq. (1) a dimensionless energy offset from the exact photon orders, $\delta_E = [E - N\hbar\omega]/\hbar\omega$, for conveniently characterizing intrasideband effects. The spectral envelope $\tilde{\Psi}_N(E)$ of the N th sideband is a replica of the initial spectral envelope $\tilde{\Psi}_0(E)$ according to $\tilde{\Psi}_N(E) = \tilde{\Psi}_0(E - N\hbar\omega)e^{iN\varphi_1}$, where $\tilde{\Psi}_0(E) = \int \Psi_0(z', 0) \exp[-iEz'/\hbar v_0] dz'$. The phase $\varphi_1 = \arg g_1$ is the injection phase, that is, the absolute phase of the first-interaction laser field at which the electron wave packet's center is located at $z = 0$. In our experiments, this phase is undefined and needs to be averaged out to predict a measured spectrum.

What are the properties of Eq. (1)? As expected from Fig. 1, the final spectrum is a double summation over the numbers of photons absorbed at the first interaction n and at the second interaction m . Negative numbers correspond to photon emission or energy loss. A particular sideband N with envelope $\tilde{\Psi}_N(E)$ is a coherent sum of all pathways with $N = n + m$ [16]. However, for extended propagation times, the wave function components at sideband number n from the first interaction acquire a nontrivial phase term $-i\Lambda(n^2 + 2n\delta_E)$ before the second interaction. This phase is linear in distance between the interactions via Λ and also

linear in energy via $2n\delta_E$. In the example of Fig. 1(b), the final zero-loss peak at $N = 0$ is composed of a zero phase slope for the *direct* component ($n = 0$, blue) but two linear and opposite phase slopes for the two *detour* components at $n = \pm 1$ (magenta and cyan). The point of constructive interference can therefore shift in the energy domain as a function of the optical phase delay φ in the phase term in Eq. (1).

To quantify the peak shifts to be observed in an experiment, we average Eq. (1) over the injection phase φ_1 via $\rho^{\text{pure}} = \int \tilde{\Psi}_f \tilde{\Psi}_f^* d\varphi_1 / (2\pi)$ and obtain

$$\rho^{\text{pure}}(E, \varphi) = \sum_N |\tilde{\Psi}_N(E)|^2 \sum_{m, m'} R_{N, m, m'} \times e^{i(m-m')[\varphi - \Lambda(m+m' - 2\delta_E - 2N)]}. \quad (2)$$

Here, variables with a prime correspond to the summation indices in $\tilde{\Psi}_f^*$ and $R_{N, m, m'} = J_{N-m}(|g_1|)J_m(|g_2|) \times J_{N-m'}(|g_1|)J_{m'}(|g_2|)$.

Figures 1(e) and 1(f) illustrate the summation of the partial components in Eq. (2) with vector diagrams for the case of equal and moderate laser intensities ($|g_1| = |g_2| \lesssim 1$) such that only the zero-loss peak (ZLP) and the first sidebands are involved ($N = 0, \pm 1$). From these diagrams, the maximum of the ± 1 sidebands in $(\delta_E; \varphi)$ coordinates is given by

$$\cos^2[(\varphi \pm \Lambda)/2 + \Lambda\delta_E] |\tilde{\Psi}_0(\delta_E \hbar \omega)|^2 \rightarrow \max. \quad (3)$$

Analogously for the ZLP (omitting the arguments of J_0 and J_1 for clarity):

$$[J_0^4 + 4J_1^4 \cos(\varphi + 2\Lambda\delta_E) - 4J_0^2 J_1^2 \cos \Lambda \cos(\varphi + 2\Lambda\delta_E)] \times |\tilde{\Psi}_0(\delta_E \hbar \omega)|^2 \rightarrow \max. \quad (4)$$

The first factor in Eqs. (3) and (4) is maximized at slanted lines $\varphi = -2\Lambda\delta_E - N\Lambda$, where $N = 0, \pm 1$ (we dropped out the 2π periodicity), and the second factor typically peaks at the sideband center $\delta_E = 0$. The competition between these factors determines the position of the peak, that is, $\delta_E^{\text{max}, N}(\varphi)$ or $\varphi_N^{\text{max}}(\delta_E)$. This peak shift depends on the particular $\tilde{\Psi}_0(\delta_E \hbar \omega)$ and thereby on τ^{pure} . For a Gaussian wave packet, we obtain for the ± 1 sidebands:

$$\varphi_{\pm 1}^{\text{max}}(\delta_E) = -2\text{atan}[(\omega\tau^{\text{pure}})^2 \Lambda^{-1} \delta_E] - 2\Lambda\delta_E \mp \Lambda. \quad (5)$$

Neglecting terms proportional to δ_E^2 and higher allows to simplify Eq. (5) to $\delta_E^{\text{max}, \pm 1}(\varphi) = -\Lambda[2(\omega\tau^{\text{pure}})^2 + \Lambda^2]^{-1} \times \tan[(\varphi \pm \Lambda)/2]$ and to obtain for the ZLP:

$$\delta_E^{\text{max}, 0}(\varphi) = \Lambda \frac{2J_1^2(J_0^2 \cos \Lambda - 2J_1^2 \cos \varphi) \sin \varphi}{(\omega\tau^{\text{pure}})^2 (J_0^4 + 4J_1^4 \cos^2 \varphi - 4J_0^2 J_1^2 \cos \varphi \cos \Lambda) + 4\Lambda^2 J_1^2 (2J_1^2 \cos 2\varphi - J_0^2 \cos \Lambda \cos \varphi)}. \quad (6)$$

We see that the shifts of the bands according to Eqs. (5) and (6) can appear only at a nonzero propagation distance $L \propto \Lambda$ and therefore not in experiments with $L \approx 0$ [26]. For a substantial and suitable L , the peak shifts depend on τ^{pure} . In case of a very small temporal coherence ($\tau^{\text{pure}} \ll \Lambda/\omega$), Eqs. (5) and (6) reduce to $\varphi_N^{\text{max}} = -2\Lambda\delta_E - N\Lambda$, where $N = 0, \pm 1$, describing the case of a linear acceleration and deceleration by the optical field cycles in the point-particle regime [17,35]. For a high coherence ($\tau^{\text{pure}} \gg \Lambda/\omega$), the peak shifts are proportional to $(\omega\tau^{\text{pure}})^{-2}$ and approach zero for infinite coherence. Analogous equations are obtained for higher-order sidebands (see Supplemental Material [34]).

Importantly, the sideband peak shifts are not sensitive to variations of the central energy as long as $N\hbar\omega \ll E_0$. An inhomogeneous spectral broadening of the beam therefore does not affect the peak shifts. Also, a prechirp of the electron wave packet before the first laser interaction is irrelevant for our results. To see this, we repeat the calculations for an initially chirped Gaussian wave packet $\Psi_0(z') = A \exp[-z'^2(1+iC)^{-1}(2v_0\tau^{\text{pure}})^{-2}]$, where C is the chirp parameter. We obtain the envelope

$\Psi_N^{\text{chirp}}(E) \propto e^{iN\varphi_1} e^{-(\tau^{\text{pure}}/\hbar)^2(E-N\hbar\omega)^2(1+iC)}$, that depends on C only via a phase term which cancels out in $\rho^{\text{pure}}(E, \varphi)$; see Eq. (2). We note that a delay-dependent energy shift of the spectrogram as a whole can occur for chirped femtosecond electron wave packets [16,36], but such a global shift does not change the energy spacing between the sidebands, in contrast to our results.

Figure 2 shows the calculated spectrograms $\rho^{\text{pure}}(E, \varphi)$ for several different electron coherences τ^{pure} . The laser period is 6.5 fs, the electron energy is $E_0 = 75$ keV, $|g_{1,2}| = 1$, and the propagation distance is $L = 13.9$ cm, corresponding to $\Lambda = \pi/2$. For an electron coherence of $\tau^{\text{pure}} = 6$ fs, the peak shift is almost unobservable [13,26], but coherences of 3 fs and below produce substantial asymmetric shifts of the sidebands that are described by Eqs. (5) and (6). At a very low coherence (1 fs), the electron approaches the point-particle regime and the spectrogram begins to show features of classical field-slope acceleration [17]. The sensitivity of the spectrograms to τ^{pure} on dimensions of a few femtoseconds is related to the small but finite propagation delay of 3.3 fs between the partial wave packets at $n = 0$ and $n = 1$ for the parameters of Fig. 2.

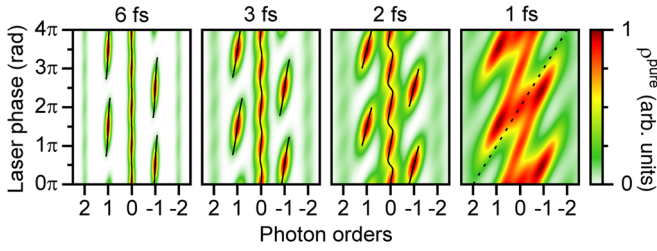


FIG. 2. Calculated time-energy spectrograms. Depending on the pure temporal coherence τ^{pure} (upper labels), sidebands acquire asymmetric energy shifts. Solid curves, calculations by Eqs. (5) and (6). For 1 fs and below, we approach the point-particle limit and classical acceleration and deceleration (dashed line).

In measurements of a realistic multielectron beam with a finite ensemble coherence, the pure spectrum of Eq. (2) needs to be convolved with the incoherent spectral broadening $\sigma_E^{\text{ens}} \approx \hbar/(2\tau^{\text{ens}})$. Assuming a Gaussian broadening,

$$\rho^{\text{meas}}(E, \varphi) = \rho^{\text{pure}}(E, \varphi) \otimes e^{-(E/\sqrt{2}\sigma_E^{\text{ens}})^2}. \quad (7)$$

Hence, τ^{pure} and τ^{ens} can be distinguished in a robust way from practical photon-order spectrograms: τ^{pure} manifests itself in symmetry-breaking photon-order peak shifts via Eqs. (5) and (6) [see Fig. 1(c)] and τ^{ens} produces a symmetric broadening of all sidebands via Eq. (7) [see Fig. 1(d)].

In the experiment, we use a Philips CM-12 transmission electron microscope with a Gatan GIF100 postcolumn energy spectrometer and establish the interferometer with the help of two laser-electron interactions at a distance of $L = 12$ cm [14]. The electron energy is $E_0 = 75$ keV. The modulation elements are thin silicon membranes that are illuminated with a single-longitudinal-mode continuous-wave laser at $\lambda = 1.95$ μm at a power of 3 W, providing $|g_{1,2}| \approx 0.3$. The temporal coherence of the electrons is varied by changing the temperature T of the microscope's

LaB₆ thermal electron emitter via the “filament” setting of the control electronics.

Figure 3(a) shows the measurement results (top panel) in comparison to a series of fits with Eq. (7) (bottom panels). For display, a laser-unaffected reference spectrum is subtracted from all datasets and fits. We observe a laser-delay-dependent variation of the intensities of the ZLP and the sidebands. In time, the sideband maxima are located at $\varphi = \pm\Lambda = \pm 0.43\pi$ with respect to the minimum of the ZLP, in accordance with Eqs. (3) and (4). Additionally, we see asymmetric shifts and tilts of the ZLP and the sideband features which increase with emitter temperature. At the same time, the sidebands become broader. Figure 3(b) shows a close-up into the -1 photon-order peaks. The model of Eq. (7) describes these experimental results qualitatively well; see the fit results in the bottom panels of Fig. 3(a). After precalibration of $|g_{1,2}|$ [14], the fits use only three remaining free parameters: τ^{pure} , τ^{ens} , and the zero position of the piezoelectric laser phase delay. Because of the different symmetry effects of τ^{pure} and τ^{ens} (see above), we can therefore reliably extract both values and obtain close-to-identical results for widely varying initial fit guesses. We note the similarity of our free-electron interferometry to the measurement of attochirp and photo-emission delays by the RABBITT principle in optical attosecond spectroscopy [37,38].

Figure 4(a) shows the measured τ^{pure} and τ^{ens} as a function of the filament current and emitter temperature. All values lie in the range of 1–4 fs (root-mean square) and decrease with increasing emission temperature. The pure coherence is always longer than the ensemble coherence for all investigated conditions. Figure 4(b) shows the full-width-at-half-maximum energy bandwidths $\Delta_E^{\text{pure}} = 2\sqrt{\ln 2}\sigma_E^{\text{pure}}$ and $\Delta_E^{\text{ens}} = 2\sqrt{\ln 2}\sigma_E^{\text{ens}}$ as well as the corresponding associated pure emission temperatures via $T = \hbar/(2\tau^{\text{pure}}k_B)$ [24]. These temperatures (magenta squares) cover the temperature range from 1000 to 2100 K, typical

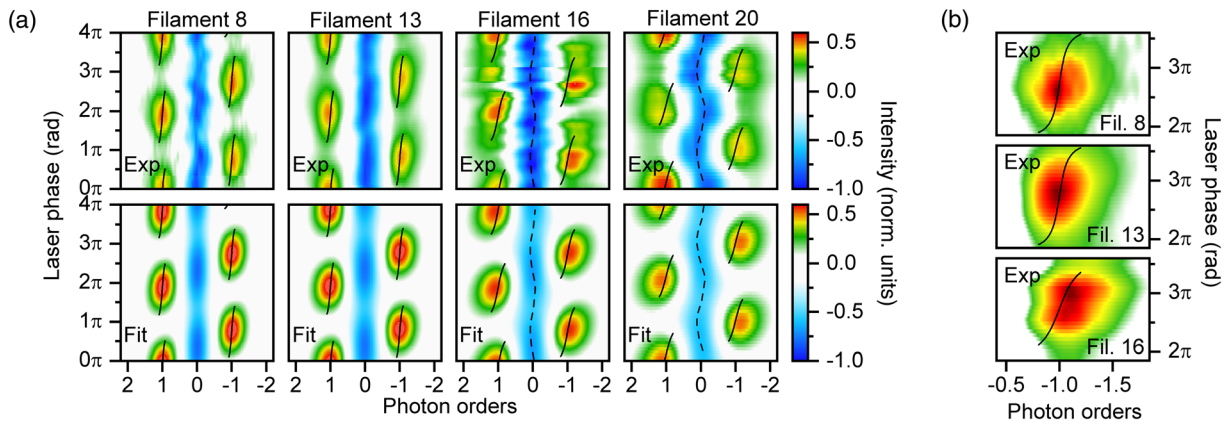


FIG. 3. Experimental observation of photon-order peak shifts and measurement of pure temporal coherence τ^{pure} . (a) Experimental data (top panels) and fits (bottom panels) for various filament currents of the emitter. Solid curves, calculation with Eq. (5). Dashed curves, calculation with Eq. (7). (b) Close-up into the experimental data. Solid curves, calculation with Eq. (5).

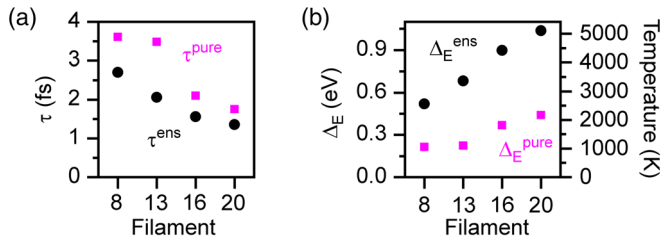


FIG. 4. Pure and ensemble coherences of a free-electron beam. (a) τ^{pure} (magenta squares) and τ^{ens} (black circles) as a function of filament current. (b) Pure energy bandwidth (magenta) and ensemble energy bandwidth (black) in relation to emission temperatures.

for LaB₆ emitters [39,40], affirming the validity of our measured τ^{pure} . In contrast, the effective temperatures of the entire beam as an ensemble (black dots) reach up to 5000 K, more than possible in an emitter material, and therefore must have another origin. The associated ensemble broadening ΔE^{ens} increases from 0.5 to 1 eV, indicating that the spectral apparatus function or other constant factors have only a partial contribution therein. We therefore attribute the growing part of ΔE^{ens} to the space-charge forces and the Boersch effect [27,29]. The LaB₆ cathode in our experiment emits a current of 70 μA from a 15- μm tip at the highest filament setting. The corresponding average distance of the electrons is $<4 \mu\text{m}$, realistic for a substantial Boersch effect but large enough to not provide wave function overlap between different electrons in the beam. We conclude that each emitted electron carries an intrinsic temporal coherence τ^{pure} that is inherited from the emitter temperature and maintained during beam propagation, but the central energy of each such electron in an ensemble fluctuates by Coulomb repulsion from nearby other electrons in the beam.

Interestingly, the pure coherence in full-width-at-half-maximum units exceeds 5 fs even for high emission currents. This result shows that nonpulsed electrons from thermal emitters have enough temporal coherence for attosecond pulse generation [13,14,26] or free-electron quantum operations [16,21,41]. The reported time-domain electron interferometry with multiple laser-electron interactions and free-space propagations can reveal the temporal properties of free-electron matter waves on the level of the isolated particles, that is, without disturbances from incoherent bandwidth effects. We see vivid perspectives of such kind of electron interferometry for attosecond materials characterizations [13], quantum electron microscopy [42], entanglement of electrons with light [22,41], studies of the dynamical Aharonov-Bohm effect [43] or real-space ultrafast electron microscopy of light-driven electronic motion in complex materials at novel time-resolution regimes [44–46].

We thank Johannes Thurner for help with the energy spectrometer and Ferenc Krausz for laboratory infrastructure.

We acknowledge funding from the Dr. K. H. Eberle Stiftung, the Vector Stiftung, the European Research Council (ERC) via Consolidator Grant 647771, and the Deutsche Forschungsgemeinschaft (DFG) via SFB1432.

*peter.baum@uni-konstanz.de

- [1] T. Nakane, A. Kotecha, A. Sente, G. McMullan, S. Masiulis, P. M. G. E. Brown, I. T. Grigoras, L. Malinauskaitė, T. Malinauskas, J. Miehlting *et al.*, Single-particle cryo-EM at atomic resolution, *Nature (London)* **587**, 152 (2020).
- [2] H. Lichte and M. Lehmann, Electron holography—Basics and applications, *Rep. Prog. Phys.* **71**, 016102 (2008).
- [3] M. Gemmi, E. Mugnaioli, T. E. Gorelik, U. Kolb, L. Palatinus, P. Boullay, S. Hovmöller, and J. P. Abrahams, 3D electron diffraction: The nanocrystallography revolution, *ACS Cent. Sci.* **5**, 1315 (2019).
- [4] P. Ercius, O. Alaidi, M. J. Rames, and G. Ren, Electron tomography: A three-dimensional analytic tool for hard and soft materials research, *Adv. Mater.* **27**, 5638 (2015).
- [5] C. Colliex, M. Kociak, and O. Stéphan, Electron energy loss spectroscopy imaging of surface plasmons at the nanometer scale, *Ultramicroscopy* **162**, A1 (2016).
- [6] B. J. Siwick, J. R. Dwyer, R. E. Jordan, and R. J. D. Miller, An atomic-level view of melting using femtosecond electron diffraction, *Science* **302**, 1382 (2003).
- [7] P. Baum, D. S. Yang, and A. H. Zewail, 4D visualization of transitional structures in phase transformations by electron diffraction, *Science* **318**, 788 (2007).
- [8] A. H. Zewail, Four-dimensional electron microscopy, *Science* **328**, 187 (2010).
- [9] R. J. D. Miller, Femtosecond crystallography with ultra-bright electrons and x-rays: Capturing chemistry in action, *Science* **343**, 1108 (2014).
- [10] A. Ryabov and P. Baum, Electron microscopy of electromagnetic waveforms, *Science* **353**, 374 (2016).
- [11] T. Frigge, B. Hafke, T. Witte, B. Krenzer, C. Streubühr, A. Samad Syed, V. M. Trontl, I. Avigo, P. Zhou, M. Ligges, D. von der Linde, U. Bovensiepen, M. Horn-von Hoegen, S. Wippermann, A. Lücke, U. Gerstmann, and W. G. Schmidt, Optically excited structural transition in atomic wires on surfaces at the quantum limit, *Nature (London)* **544**, 207 (2017).
- [12] E. Pomarico, Y.-J. Kim, F. J. G. de Abajo, O.-H. Kwon, F. Carbone, and R. M. van der Veen, Ultrafast electron energy-loss spectroscopy in transmission electron microscopy, *MRS Bull.* **43**, 497 (2018).
- [13] Y. Morimoto and P. Baum, Diffraction and microscopy with attosecond electron pulse trains, *Nat. Phys.* **14**, 252 (2018).
- [14] A. Ryabov, J. W. Thurner, D. Nabben, M. V. Tsarev, and P. Baum, Attosecond metrology in a continuous-beam transmission electron microscope, *Sci. Adv.* **6**, eabb1393 (2020).
- [15] B. Barwick, D. J. Flannigan, and A. H. Zewail, Photon-induced near-field electron microscopy, *Nature (London)* **462**, 902 (2009).
- [16] A. Feist, K. E. Echternkamp, J. Schauss, S. V. Yalunin, S. Schäfer, and C. Ropers, Quantum coherent optical phase modulation in an ultrafast transmission electron microscope, *Nature (London)* **521**, 200 (2015).

- [17] C. Kealhofer, W. Schneider, D. Ehberger, A. Ryabov, F. Krausz, and P. Baum, All-optical control and metrology of electron pulses, *Science* **352**, 429 (2016).
- [18] O. Kfir, H. Lourenço-Martins, G. Storeck, M. Sivis, T. R. Harvey, T. J. Kippenberg, A. Feist, and C. Ropers, Controlling free electrons with optical whispering-gallery modes, *Nature (London)* **582**, 46 (2020).
- [19] K. Wang, R. Dahan, M. Shentais, and I. Kaminer, Coherent interaction between free electrons and a photonic cavity, *Nature (London)* **582**, 50 (2020).
- [20] M. T. Hassan, J. S. Baskin, B. Liao, and A. H. Zewail, High-temporal-resolution electron microscopy for imaging ultrafast electron dynamics, *Nat. Photonics* **11**, 425 (2017).
- [21] I. Madan, G. M. Vanacore, S. Gargiulo, T. LaGrange, and F. Carbone, The quantum future of microscopy: Wave function engineering of electrons, ions, and nuclei, *Appl. Phys. Lett.* **116**, 230502 (2020).
- [22] A. Karnieli, N. Rivera, A. Arie, and I. Kaminer, The coherence of light is fundamentally tied to the quantum coherence of the emitting particle, *Sci. Adv.* **7**, eabf8096 (2021).
- [23] A. Ben Hayun, O. Reinhardt, J. Nemirovsky, A. Karnieli, N. Rivera, and I. Kaminer, Shaping quantum photonic states using free electrons, *Sci. Adv.* **7**, eabe4270 (2021).
- [24] D. B. Williams and C. B. Carter, *Transmission Electron Microscopy* (Springer, New York, 2009).
- [25] P. Baum, On the physics of ultrashort single-electron pulses for time-resolved microscopy and diffraction, *Chem. Phys.* **423**, 55 (2013).
- [26] K. E. Priebe, C. Rathje, S. V. Yalunin, T. Hohage, A. Feist, S. Schäfer, and C. Ropers, Attosecond electron pulse trains and quantum state reconstruction in ultrafast transmission electron microscopy, *Nat. Photonics* **11**, 793 (2017).
- [27] M. S. Bronsgeest, J. E. Barth, G. A. Schwind, L. W. Swanson, and P. Kruit, Extracting the Boersch effect contribution from experimental energy spread measurements for Schottky electron emitters, *J. Vac. Sci. Technol. B* **25**, 2049 (2007).
- [28] P. Sonntag and F. Hasselbach, Measurement of Decoherence of Electron Waves and Visualization of the Quantum-Classical Transition, *Phys. Rev. Lett.* **98**, 200402 (2007).
- [29] M. Kuwahara, Y. Nambo, K. Aoki, K. Sameshima, X. Jin, T. Ujihara, H. Asano, K. Saitoh, Y. Takeda, and N. Tanaka, The Boersch effect in a picosecond pulsed electron beam emitted from a semiconductor photocathode, *Appl. Phys. Lett.* **109**, 013108 (2016).
- [30] J.-T. Hsiang and L. H. Ford, External Time-Varying Fields and Electron Coherence, *Phys. Rev. Lett.* **92**, 250402 (2004).
- [31] P. Schattschneider and S. Löffler, Entanglement and decoherence in electron microscopy, *Ultramicroscopy* **190**, 39 (2018).
- [32] M. Nicklaus and F. Hasselbach, Wien filter: A wave-packet-shifting device for restoring longitudinal coherence in charged-matter-wave interferometers, *Phys. Rev. A* **48**, 152 (1993).
- [33] A. Gover and Y. Pan, Dimension-dependent stimulated radiative interaction of a single electron quantum wavepacket, *Phys. Lett. A* **382**, 1550 (2018).
- [34] See Supplemental Material at <http://link.aps.org/supplemental/10.1103/PhysRevLett.127.165501> for the derivation of Eq. (1) and consideration of some special cases.
- [35] Y. M. Pan, B. Zhang, and A. Gover, Anomalous Photon-Induced Near-Field Electron Microscopy, *Phys. Rev. Lett.* **122**, 183204 (2019).
- [36] F. O. Kirchner, A. Gliserin, F. Krausz, and P. Baum, Laser streaking of free electrons at 25 keV, *Nat. Photonics* **8**, 52 (2014).
- [37] P. M. Paul, E. S. Toma, P. Breger, G. Mullot, F. Augé, P. Balcou, H. G. Muller, and P. Agostini, Observation of a train of attosecond pulses from high harmonic generation, *Science* **292**, 1689 (2001).
- [38] H. G. Muller, Reconstruction of attosecond harmonic beating by interference of two-photon transitions, *Appl. Phys. B* **74**, s17 (2002).
- [39] P. H. Schmidt, L. D. Longinotti, D. C. Joy, S. D. Ferris, H. J. Leamy, and Z. Fisk, Design and optimization of directly heated LaB₆ cathode assemblies for electron-beam instruments, *J. Vac. Sci. Technol.* **15**, 1554 (1978).
- [40] ES-423E extended life LaB₆ cathode user information, <https://www.kimballphysics.com/lab6-user-information>.
- [41] O. Kfir, Entanglements of Electrons and Cavity Photons in the Strong-Coupling Regime, *Phys. Rev. Lett.* **123**, 103602 (2019).
- [42] P. Kruit, R. Hobbs, C.-S. Kim, Y. Yang, V. Manfrinato, J. Hammer, S. Thomas, P. Weber, B. Klopfer, C. Kohstall, T. Juffmann, M. Kasevich, P. Hommelhoff, and K. Berggren, Designs for a quantum electron microscope, *Ultramicroscopy* **164**, 31 (2016).
- [43] K. J. Mohler, D. Ehberger, I. Gronwald, C. Lange, R. Huber, and P. Baum, Ultrafast electron diffraction from nanophotonic waveforms via dynamical Aharonov-Bohm phases, *Sci. Adv.* **6** (2020).
- [44] V. S. Yakovlev, M. I. Stockman, F. Krausz, and P. Baum, Atomic-scale diffractive imaging of sub-cycle electron dynamics in condensed matter, *Sci. Rep.* **5**, 14581 (2015).
- [45] Y. Morimoto, Y. Shinohara, M. Tani, B.-H. Chen, K. L. Ishikawa, and P. Baum, Asymmetric single-cycle control of valence electron motion in polar chemical bonds, *Optica* **8**, 382 (2021).
- [46] S. T. Park, M. Lin, and A. H. Zewail, Photon-induced near-field electron microscopy (PINEM): Theoretical and experimental, *New J. Phys.* **12**, 123028 (2010).